Characteristics of global precipitable water in ENSO events revealed by COSMIC measurements

Wen-Hsin Teng,[1] Ching-Yuang Huang,[1,2] Shu-Peng Ho,[3] Ying-Hwa Kuo,[3] and Xin-Jia Zhou[3]

Received 17 August 2012; revised 25 March 2013; accepted 26 March 2013; published 15 August 2013.

[1] Precipitable water (PW) retrievals from FORMOSAT-3/Constellation Observing System for Meteorology, Ionosphere, and Climate (COSMIC) Global Positioning System (GPS) radio occultation (RO) measurements were analyzed and compared with those derived from Special Sensor Microwave/Imager (SSM/I) and Advanced Microwave Scanning Radiometer for Earth Observation System (AMSR-E) during the El Niño-Southern Oscillation (ENSO) events from 2007 to 2011. For the three ENSO events in 2007–2011, monthly mean binned COSMIC PW results are in a very high correlation (up to 0.98) with those of SSM/I and AMSR-E over the ocean, generally with root-mean-square differences less than 4 mm. PW retrievals from the three satellites are also of similar latitudinal variations. However, the PW is slightly underestimated by GPS RO, in particular, in the tropical regions. This underestimate may be caused partially by the fact that not all RO measurements can reach the surface. Inter-satellite PW anomaly comparisons for the winter months in the ENSO events, with respect to those during the neutral (non-ENSO) months, show consistent ENSO signals with major PW anomaly near the central Pacific in the warm event and near the Indonesian region and east of Australia in the two cold events. However, the 2007/2008 La Niña is somewhat less correlated for COSMIC with AMSR-E and SSM/I. For the stronger 2010/2011 La Niña, their PW anomalies are in higher correlations of about 0.8.

Citation: Teng, W.-H., C.-Y. Huang, S.-P. Ho, Y.-H. Kuo, and X.-J. Zhou (2013), Characteristics of global precipitable water in ENSO events revealed by COSMIC measurements, *J. Geophys. Res. Atmos.*, *118*, 8411–8425, doi:10.1002/jgrd.50371.

1. Introduction

[2] With a global coverage, satellite observations are very useful to monitor global atmospheric variations. Satellite observations have long been utilized to retrieve high-quality temperature, humidity profiles, and global precipitable water (PW). Because Global Positioning System (GPS) radio occultation (RO) measurements are of long-term stability, little affected by rain and clouds, and are not prone to drifts in measurements among missions, the derived atmospheric profiles from GPS RO data are proven to be useful for various climate and meteorological applications [*Ware et al*., 1996; *Kursinski et al*., 1997; *Hajj et al*., 2004; *Ho et al*., 2007a, 2009a, 2010a; *Anthes et al*., 2008; *Arndt et al*., 2010; *Anthes*, 2011; *Steiner et al*., 2011]. However, so far, most studies on meteorological and climate variability used RO bending angle, refractivity, and dry atmospheric parameters rather than water vapor profiles.

[3] Launched in 2006, FORMOSAT-3/Constellation Observing System for Meteorology, Ionosphere, and Climate (hereafter, COSMIC) is a GPS RO mission which provides global atmospheric temperature and water vapor profiles [*Anthes et al*., 2008; *Ho et al*., 2010b]. With about ~2500 GPS RO soundings per day since launch, COSMIC data are distributed uniformly in time and space [*Anthes et al*., 2008]. Using the open-loop tracking technique, up to 90% of the total of COSMIC RO profiles can reach the lowest 2 km of the troposphere [*Sokolovskiy et al*., 2006]. Highly reliable moisture profiles can be retrieved from RO measurements at variable vertical resolutions of about a few hundred meters in the lower troposphere [*Kursinski et al*., 1997; *Ho et al*., 2007b, 2010a, 2010b]. The horizontal resolution of RO data is approximately 300 km [*Kursinski et al*., 1997].

[4] *Wick et al*. [2008] showed a good agreement in PW between retrievals from COSMIC RO and Defense Meteorological Satellite Program (DMSP) Special Sensor Microwave/Imager (SSM/I) in regions associated with atmospheric river phenomena off California. Comparing vertical water vapor profiles derived from RO observations and those derived from Atmospheric Infrared Sounder (AIRS), *Chou et al*. [2009] indicated that the zonal mean differences of their profiles are within 20% over tropical Pacific regions. In addition, *Ho et al*. [2010a] compared the global water vapor profiles between ECMWF (European Centre for Medium-Range Weather Forecasts) analysis and COSMIC RO observations collocated near radiosonde stations over lands during a

[1]Department of Atmospheric Sciences, National Central University, Jhong-Li, Taiwan.
[2]GPS Science and Application Research Center, National Central University, Jhong-Li, Taiwan.
[3]University Corporation for Atmospheric Research, Boulder, Colorado, USA.

Corresponding author: C.-Y. Huang, Department of Atmospheric Sciences, National Central University, Jhong-Li, Taiwan. (hcy@atm.ncu.edu.tw)

2169-897X/13/10.1002/jgrd.50371

period from July to November 2006 when COSMIC data were not included in the ECWMF analysis. Results show that COSMIC and ECMWF water vapor profiles agree within 0.05 g kg^{-1} above 2 km and 0.2 g kg^{-1} below 2 km. This demonstrates the usefulness of COSMIC RO observations in monitoring global water vapor variations.

[5] Originating from atmosphere-ocean interaction and in a cycle of 3 to 7 years, El Niño-Southern Oscillation (ENSO) has a significant impact on global climate variations and local weather patterns. For sea surface temperature (SST) over the central Pacific, the warm phase of ENSO (El Niño) is often followed by the cold phase of ENSO (La Niña). Both El Niño and La Niña take place around summer seasons in the Northern Hemisphere and reach their climax in winters. Using satellite data and observations from in situ radiosonde stations, *Rasmusson and Carpenter* [1982] demonstrated that the evolution of an ENSO event is highly correlated with the variation of SST, wind, and precipitation and is directly linked to atmospheric convection. Different surface evaporation rates and atmospheric convection, which result in significant water vapor variation, occur during different ENSO phases.

[6] Despite local and regional comparisons between COSMIC water vapor profiles and in situ observations [*Ho et al*., 2010a] and other satellite data [e.g., *Wick et al*., 2008; *Chou et al*., 2009], global and long-term assessments of COSMIC PW over remote oceans, especially during ENSO events, are still unavailable. Although *Mears et al*. [2010, 2012] found that PW of COSMIC RO and the combined PW from multiple microwave imagers exhibit similar trends over global oceans during both the warm and cold ENSO events from 2006 to 2011, detailed assessments have not yet been done.

[7] The GPS RO is a limb view remote sensing technique that uses the GPS receivers onboard low-earth-orbit (LEO) satellites, which are used to track radio signals emitted from GPS satellites. This results in vertical drifts (or smearing effects) of the RO tangent point by about 80 km from the lower troposphere to the tropopause as seen in the retrieved profiles (http://www.cosmic.ucar.edu/). When the sensing signals (excess phases) take a form of bending angles under local spherical symmetry [*Kursinski et al*., 2000], the measurements in fact account for the integrated effects along a ray path. Furthermore, in the environment of large vertical gradients, superrefraction may occur and tend to cause sizable biases in retrieving bending angle and thus refractivity [*Sokolovskiy et al*., 2003]. The retrieved refractivity from the Abel transform of a bending angle profile is also based on spherical symmetry assumption. A brief review of the GPS RO measurement technique was given by *Kursinski et al*. [2000] and *Healy et al*. [2007].

[8] On the other hand, both SSM/I and AMSR-E (Advanced Microwave Scanning Radiometer for Earth Observation System) take nadir measurements with a typical horizontal resolution of several tens of kilometers, from the surface to the satellite height. Although GPS RO and SSM/I are using different measurement techniques, *Wick et al*. [2008] found that the differences in collocated PW results from COSMIC and SSM/I west of California during two atmospheric river events were small (with root-mean-square errors of 2 mm to 4 mm), and their correlations are very high, with little influence caused by the variation of the lowest RO perigee heights (below which global model analysis was used to extrapolate). The SSM/I and AMSR-E PW from Remote Sensing System (RSS) are compared in this study. Because only gridded monthly mean SSM/I and AMSR-E PW data are available from RSS [*Wentz*, 1993, 1997; *Sohn and Smith*, 2003; *Wick et al*., 2008], in this study we will not focus on the verification of point or collocated comparisons. Rather, the comparisons will be based on averaged PW values at a seasonal mean.

[9] In light of the helpful complementary information provided by GPS RO observations for climate variability, we further looked into the gross features of PW on the globe, using the GPS RO observations from COSMIC from 2007 to 2011. This study is the first attempt to characterize the global PW distributions from COSMIC during the ENSO events and conduct inter-satellite PW comparisons especially over oceans. The 5 year RO data cover three ENSO events (one El Niño and two La Niña). We validate GPS RO PW against those from SSM/I and AMSR-E. Different kinds of data used in this study are described in section 2. The characteristic features of global circulation and PW associated with the ENSO events are given in section 3. The comparisons among PW derived from COSMIC RO and the other two satellites will be presented in section 4. The monthly mean SSM/I and AMSR-E PW from RSS are compared in this study. The causes of the differences due to different methods to extrapolate the water vapor values below the lowest penetration heights are also discussed in section 4. Comparisons on inter-satellite PW anomalies for the winter months in the ENSO events, with respect to neutral (non-ENSO) months, are conducted in section 5. Finally, our concluding remarks are given in section 6.

2. The Data and Methodology

[10] The data used in this study are GPS RO retrieved specific humidity, SSM/I, and AMSR-E estimated PWs in 2007–2011. Since 15 April 2006, COSMIC GPS RO measurements have been collected from six low-earth-orbit satellites (LEOs) which are in orbital heights from 700 km to 800 km. This constellation observation network provides a rather even global distribution with approximately 2000 daily profiles at about 300 km horizontal resolution. The raw data from RO measurements are phase delays along a ray path and can be processed to obtain bending angles [*Kursinski et al*., 2000]. Under the spherical symmetry assumption, the observed bending angles can be converted to refractivity (N), which is a function of total pressure (P) in hectopascal, temperature (T) in Kelvin, and water vapor pressure (P_w) in hectopascal [*Bean and Dutton*, 1966] given by

$$N = 77.6\frac{p}{T} + 3.73 \times 10^5 \frac{p_w}{T^2} \quad (1)$$

[11] In this study, the refractivity profiles were obtained from real-time processed data which are interpolated up to 40 km at a 100 m vertical resolution. Using refractivity profiles, water vapor profiles (wet profiles—wetPrf) can be retrieved in COSMIC/CDAAC (COSMIC Data Analysis and Archive Center) with auxiliary temperature and moisture from NCEP (National Centers for Environmental

Table 1. The Annual Number of COSMIC RO Measurement During 2007–2011 With Respect to Perigee Heights[a]

Year	2007	2008	2009	2010	2011
Total amounts	639,033	649,588	646,551	493,204	412,811
Perigee height < 3 km	614,916	634,212	632,811	481,987	403,251
	(96.2%)	(97.6%)	(97.9%)	(97.7%)	(97.7%)
Perigee height < 2 km	582,443	604,259	603,341	457,774	383,368
	(91.1%)	(93.0%)	(93.3%)	(92.8%)	(92.9%)
Perigee height < 1 km	465,941	486,337	485,766	367,146	307,833
	(72.9%)	(74.9%)	(75.1%)	(74.4%)	(74.6%)

[a]The percentage in the parentheses indicates the fraction of the total amounts.

Prediction) GFS (Global Forecast System) global forecast used as background in one-dimensional variation (1D-Var) adjustment [*Kuo et al*., 2004]. Note that neither SSM/I nor AMSR-E radiances were assimilated operationally in the NCEP GFS. Similar 1D-Var data assimilation approach to derive atmospheric states from RO refractivity observations can also be found in *Healy and Eyre* [2000] and *von Engeln and Nedoluha* [2005]. In 1D-Var, the adjustment of the atmospheric state depends on the relative observation sensitivity of refractivity to temperature and moisture, as well as the observational errors [*Ho et al*., 2007b]. In the upper and middle troposphere, the information of refractivity is mainly used to retrieve temperature. In the lower troposphere, because RO refractivity is more sensitive to water vapor variation than to the temperature [*Ho et al*., 2007b], the information of COSMIC refractivity is mainly used to derive water vapor retrievals. The COSMIC water vapor retrieval errors in the lower troposphere are mainly attributable to the uncertainty of temperature a priori where 1 K of temperature error will introduce less than 0.25 g/kg of water vapor bias in the troposphere. The detailed description of the 1D-Var algorithm used in CDAAC is documented in http://cosmic-io.cosmic.ucar.edu/cdaac/doc/documents/1dvar.pdf. The CDAAC RO inversion algorithms and the estimations of data quality are detailed in *Ho et al*. [2009b, 2012]. GPS RO refractivity errors appear to be small, ranging from 0.3% to 0.5% above 5 km when compared to those computed from both NCEP and ECMWF reanalyses [*Kuo et al*., 2004].

[12] Superrefraction in the boundary layer may cause negative N bias which leads to biases in retrieved temperature as well as humidity in the lower troposphere. What we used from CDAAC in this study is the vertical RO humidity sounding above the lowest ray perigee point. The accuracy of COSMIC derived PW has been demonstrated by comparisons with PW derived from ground-based GPS (i.e., International Global Navigation Satellite Systems–IGS, *Wang et al*. [2007]) in *Ho et al*. [2010b]. The mean global difference between IGS (mainly over lands) and COSMIC PW is about −0.17 mm with a standard deviation of 2.73 mm. The correlation coefficient is as high as 0.97. In this study, we extend the comparison of COSMIC PW and the PWs retrieved from other SSM/I and AMSR-E over ocean. Table 1 lists the total number of the available COSMIC RO profiles for each year from 2007 to 2011 with the lowest ray perigee heights below 3 km, 2 km, and 1 km, respectively. Roughly, the average RO sample number is around 1800 per day in 2008, then drops by about 24.1% in 2010 and about 36.5% in 2011. Almost 96% (91%) of the RO measurements (after some quality checks imposed by CDAAC) can penetrate to below 3 km (2 km) but retains only about 73% for the lowest ray perigee heights below 1 km.

[13] For having reasonable inter-satellite PW comparisons, we only use the available RO measurements with the ray perigee heights below 1 km. To calculate COSMIC PW, we integrate the specific humidity upward from the lowest tangent point (i.e., ray perigee height) to the retrieved maximum height (40 km) and compensate the layer of void data from the lowest ray perigee height to the surface by filling the same water vapor value obtained at the lowest perigee height. Note that because the lowest ray perigee heights (i.e., below 1 km) may occur more often in drier atmosphere (or drier regions) than in wetter atmosphere (or wetter regions), this approach may introduce sampling errors relative to the true atmosphere. In addition, different methods to extrapolate the water vapor values below the lowest penetration heights may also introduce extra PW uncertainty. The combined sampling error uncertainty and the effect of extrapolating the water vapor values below the lowest penetration heights may introduce less than on average about 2 mm PW biases (see section 4 for more discussions).

[14] For a comparison purpose, the PW data are binned into 72×36 global grids (e.g., in a $5^\circ \times 5^\circ$ resolution) close to the horizontal resolution of RO data (at low latitudes, the horizontal resolution is distinctively smaller than 5°). To see how the COSMIC PWs are correlated with other atmospheric variables during ENSO events, we also compared the binned COSMIC PW with those from NCEP global reanalysis [*Kalnay et al*., 1996], the gridded global precipitation rate from Global Precipitation Climatology Project (GPCP), and NOAA optimal interpolated (OI) SST.

[15] In this study, PW retrievals from the two passive microwave radiometric systems, SSM/I and AMSR-E, were taken from RSS. Onboard the DMSP F15 satellite, SSM/I utilizes seven microwave frequency channels (19.35, 37.0, 85.5 GHz with dual-polarization; 22.235 GHz with V-polarization only) with a scanned swath of about 1400 km in width. AMSR-E instrument is onboard the NASA Aqua satellite. AMSR-E uses 12 microwave frequency channels (6.9 GHz to 89.0 GHz with dual-polarization) with a scanned swath of about 1445 km in width (http://www.remss.com). SSM/I and AMSR-E PWs obtained from RSS are available in $0.25^\circ \times 0.25^\circ$ grids. For a comparison purpose, we averaged all the SSM/I and AMSR-E PWs into $5^\circ \times 5^\circ$ grids. Note that since SSM/I and AMSR-E data are collected from fixed local times, this may contribute to sampling error uncertainty in the comparisons among COSMIC and SSM/I and AMSR-E PWs. In this study, we assume the (regional) diurnal variation of PW over oceans is reasonably small.

Table 2. Oceanic Nino Index (ONI) for 2006–2012[a]

Year	Dec–Feb	Jan–Mar	Feb–Apr	Mar–May	Apr–Jun	May–Jul	Jun–Aug	Jul–Sep	Aug–Oct	Sep–Nov	Oct–Dec	Nov–Jan
2006	**−0.9**	**−0.7**	**−0.5**	−0.3	0.0	0.1	0.2	0.3	**0.5**	**0.8**	**1.0**	**1.0**
2007	**0.7**	0.3	−0.1	−0.2	−0.3	−0.3	−0.3	**−0.6**	**−0.9**	**−1.1**	**−1.2**	**−1.4**
2008	**−1.5**	**−1.5**	**−1.2**	**−0.9**	**−0.7**	**−0.5**	−0.3	−0.2	−0.1	−0.2	−0.4	−0.7
2009	−0.9	−0.8	−0.6	−0.2	0.1	0.4	**0.5**	**0.6**	**0.7**	**1.0**	**1.4**	**1.6**
2010	**1.6**	**1.4**	**1.1**	**0.7**	0.2	−0.3	**−0.8**	**−1.2**	**−1.4**	**−1.5**	**−1.5**	**−1.5**
2011	**−1.4**	**−1.3**	**−1.0**	**−0.7**	−0.4	−0.2	−0.2	−0.3	**−0.6**	**−0.8**	**−1.0**	**−1.0**
2012	**−0.9**	**−0.7**	**−0.5**	−0.3	−0.1	0.0	0.1	0.3	0.4	-	-	-

[a]Covering the major COSMIC measurement period of 2006–2011. The ONI is defined as the anomaly of 3 month averaged SST over the Niño 3.4 (5°N–5°S, 120°W–170°W) with respect to the climate average (1971–2000). El Niño (La Niña) is indicated by bold ONI above (below) +0.5 (−0.5) for successive five overlapping seasons. (http://www.cpc.ncep.noaa.gov/products/analysis_monitoring/ensostuff/ensoyears.shtml).

3. Global Zonal and Spatial COSMIC PW Distributions During the ENSO Warm and Cold Events

[16] Seasonal and latitudinal variations of COSMIC PW from 2007 to 2011 are shown in this section. During this time period, there was one warm event (El Niño) from July 2009 to April 2010 and two cold events (La Niña) from August 2007 to June 2008 and from July 2010 to April 2011, respectively. Based on the Ocean Nino Index (ONI) for 2006–2012 (Table 2) obtained from NOAA Climate Prediction Center (CPC) (see http://www.cpc.ncep.noaa.gov), El Niño (La Niña) is defined when the 3 month (season) averaged SST over the Niño 3.4 region (5°N–5°S, 120°–170°W) is 0.5°C higher (lower) than the climate average (1971–2000) for successive five overlapping seasons. As shown in Table 2, both El Niño and La Niña are reaching higher SST anomalies during the winter time. The warm ENSO event during this study period (from 2007 to 2011) is the strongest El Niño event in the last decade (from 2000 to 2010). Herein, we present the variation of COSMIC PW during the 2007/2008 cold event and 2009/2010 warm event and compare COSMIC PW with those from

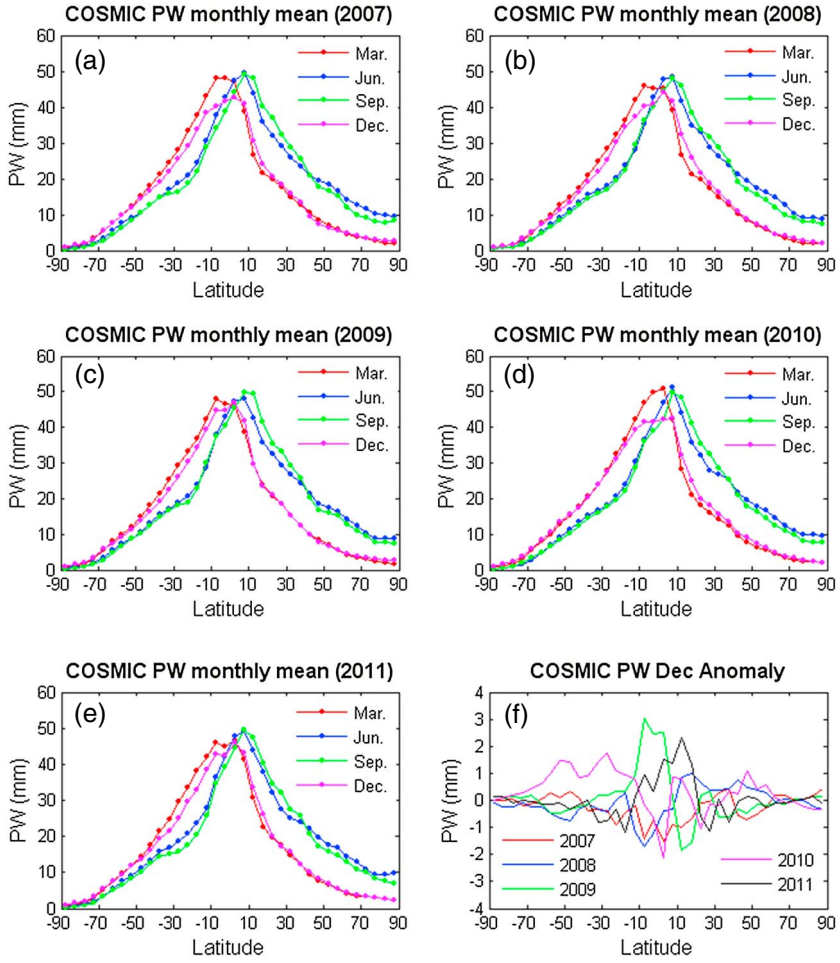

Figure 1. Zonal mean distributions of COSMIC PW (mm) in different latitudinal zones for monthly mean at March (red), June (blue), September (green), and December (pink) in (a) 2007, (b) 2008, (c) 2009, (d) 2010, and (e) 2011. (f) Anomaly of zonal mean PW in December from 2007 to 2011 averages.

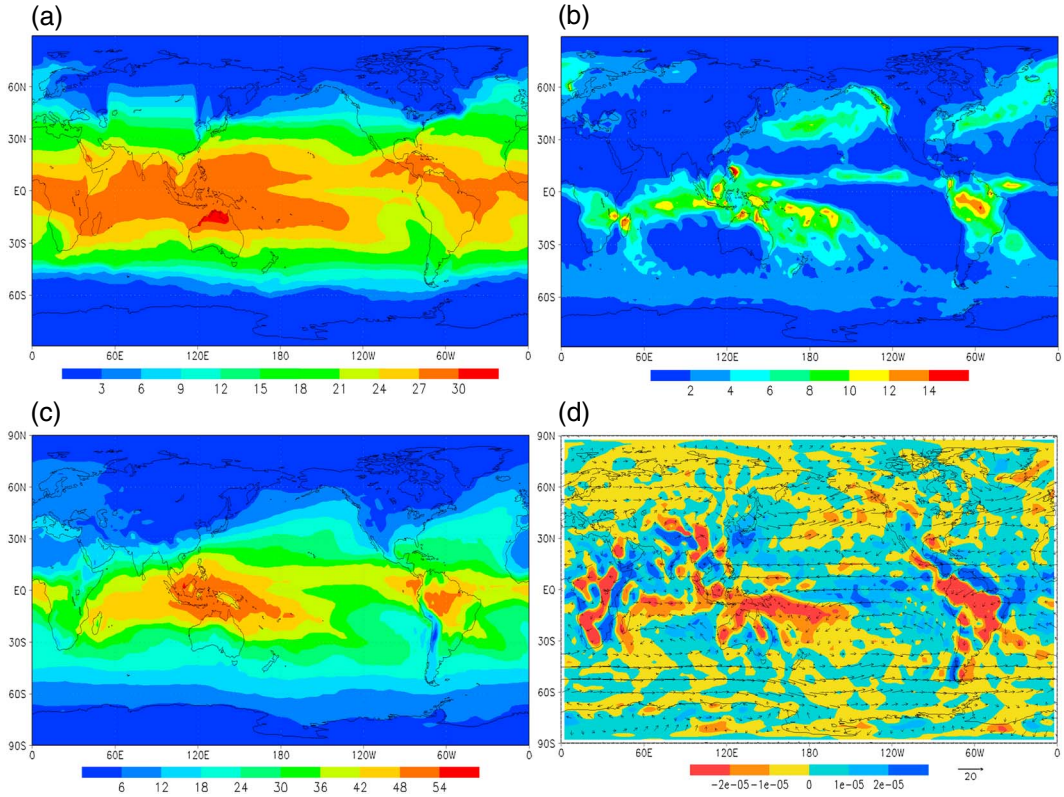

Figure 2. Seasonal average of the winter months from December 2007 to February 2008 (the cold ENSO event) for (a) sea surface temperature (°C), (b) precipitation rate (mm d^{-1}), (c) NCEP PW (mm), and (d) the horizontal divergence of water vapor flux (g kg^{-1} s^{-1}) (color shape) and horizontal wind (m s^{-1}) at 850 hPa.

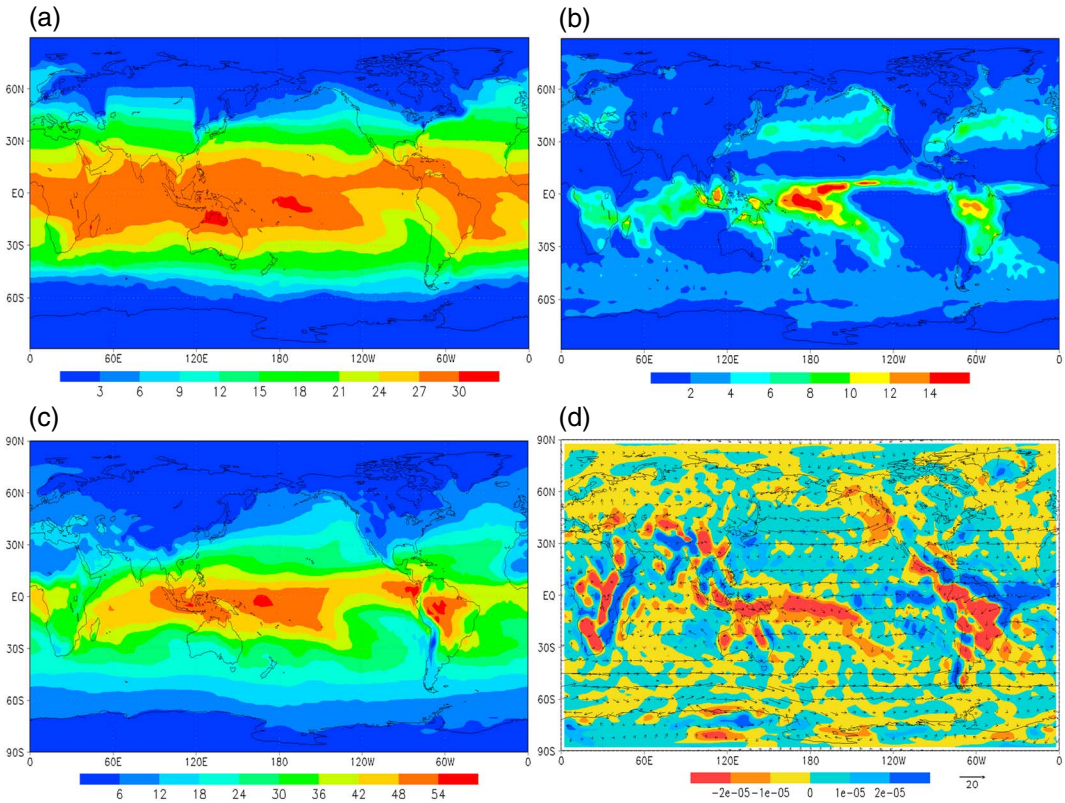

Figure 3. As in Figure 2 but from December 2009 to February 2010 (the warm ENSO event).

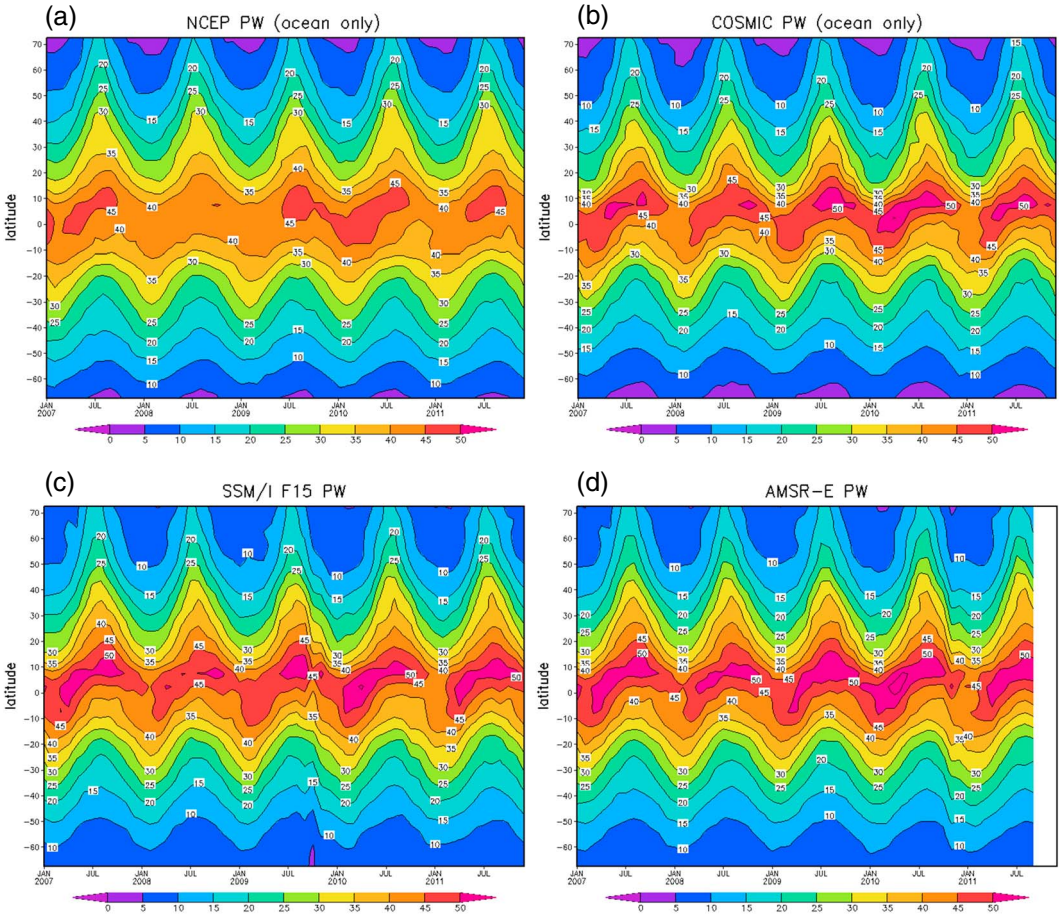

Figure 4. Latitudinal variations of monthly mean PW (mm) in 2007–2011 for (a) NCEP global reanalysis, (b) COSMIC, (c) SSM/I, and (d) AMSR-E. Note that the data for AMSR-E are available only before September 2011 as seen in Figure 4d.

other global observations for the winter time only. Because the COSMIC PW variation in 2010/2011 cold event is very similar to that of the 2007/2008 cold event, we just present the PW comparison results from the 2007/2008 cold event.

3.1. Global Variation of Mean Latitudinal COSMIC PW

[17] We first group the COSMIC PW in zonal bins of 5° latitudinal width (i.e., 36 bins). Figure 1 depicts the latitudinal variation of 5° binned monthly mean COSMIC PW for March, June, September, and December from 2007 to 2011 representing the seasonal variation during (the Northern Hemisphere) spring, summer, fall, and winter, respectively. In general, high PW occurs in the tropics and low PW occurs at high latitudes. The peak of the zonal mean PW follows the seasonal variation of the Intertropical Convergence Zone (ITCZ). The location of the maximum binned PW (~48–49 mm) occurs at 10°S in March and migrates over the equator to 5°N in June, further advances northward to about 7.5°N in September, and then returns to the equator in December. The latitudinal variations are of similar magnitude from 2007 to 2011 (Figures 1a–1e).

[18] Figure 1f depicts the latitudinal variations of averaged PW anomalies in December for each year relative to the averaged December PW from 2007 to 2011. The PW anomalies for each year are within 3 mm, with alternating positive and negative anomalies mainly in the south tropics. Note that the latitudinal variations also include PW over lands. We found that the latitudinal variations of ocean-only PW anomalies are similar to those in Figure 1f except for midlatitudes in the Northern Hemisphere (not shown). For the strongest month of two cold events in 2007 and 2010, most of the tropical regions are dominated by negative PW anomalies, while the largest positive PW anomalies are present in December 2009 for the warm event. For the neutral condition in December 2008, the PW anomalies are moderately negative and positive about south and north of the equator, respectively. In particular, a significant positive phase is present in the tropics in December 2011 with a peak near 10°N. The reason for the large positive PW anomalies in the north tropics for December 2011 is worthy of investigation.

3.2. The 2007/2008 La Niña (Cold Event)

[19] The 2007/2008 La Niña event was the first cold ENSO event during the COSMIC measurement period. To highlight the corresponding atmospheric convection during the 2007/2008 La Niña event and to compare atmosphere convection with the spatial COSMIC PW distribution (in $5° \times 5°$ grids), we depicted the seasonal average of the winter months from December 2007 to February 2008 (the most intense phase of the cold event) for SST and PW computed from the NCEP reanalysis in Figure 2.

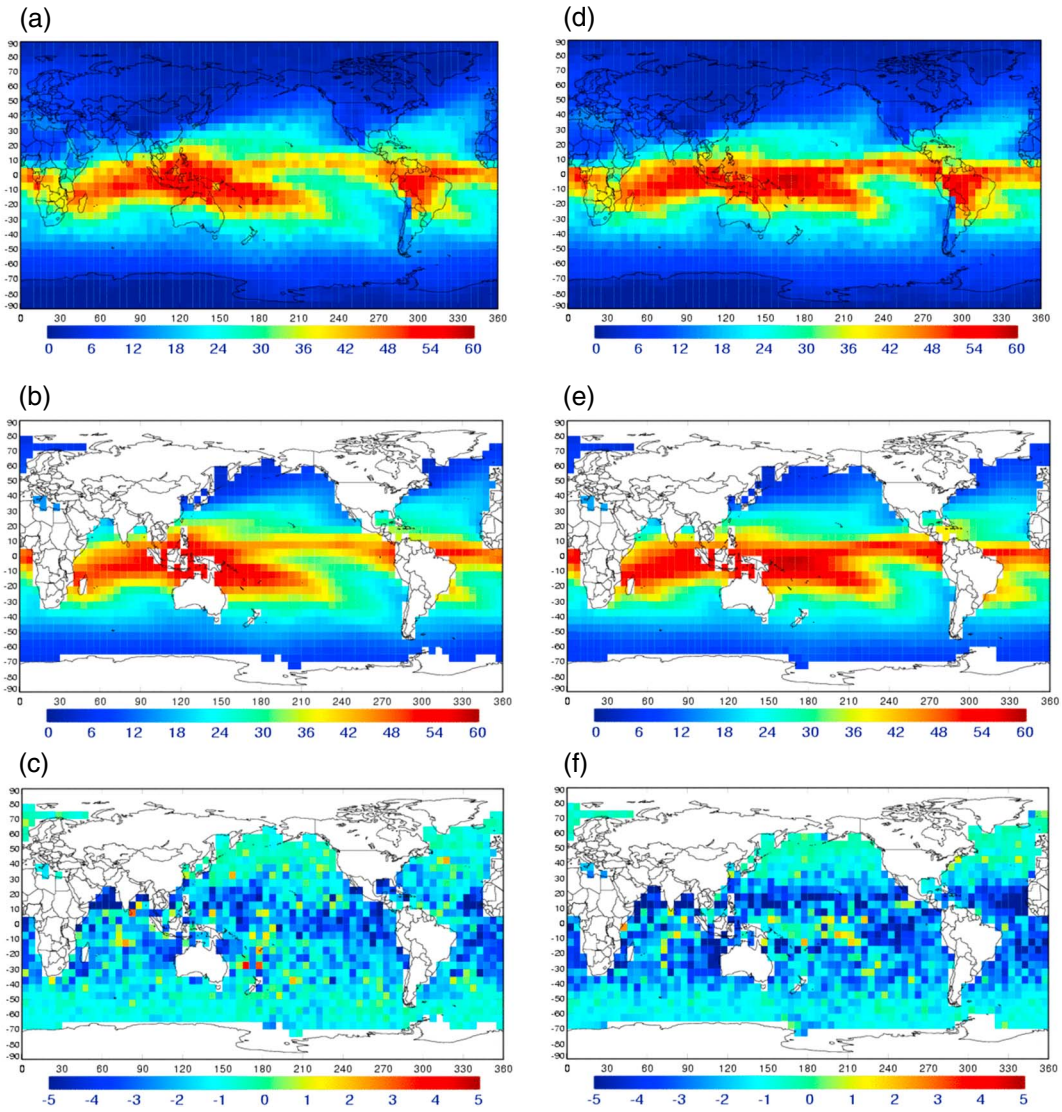

Figure 5. Seasonal average of PW (mm) at bins in the winter months for (a) the cold event (December 2007 to February 2008) for COSMIC, (b) as in Figure 5a but for AMSR-E, and (c) for the differences in PW between COSMIC and AMSR-E; (d, e, and f) as in Figures 5a, 5b, and 5c, respectively, but for the warm event (December 2009 to February 2010).

The horizontal divergence of water vapor flux and horizontal wind at 850 hPa are also computed using the NCEP reanalysis. For this La Niña event, higher precipitation rate occurs close to Indonesian regions, which is consistent with westward shifted higher SST and higher NCEP reanalysis PW compared to adjacent regions. The accompanied equatorial easterly wind, as seen in Figure 2d, advances more westward to induce a convergence zone of horizontal water vapor flux which is consistent with the distribution of high NCEP PW (Figure 2c). These tropical variations of different observations and NCEP global reanalyses are in a good agreement. Strong vertical convection is observed over Amazon (Figures 2a–2d), which is also of high COSMIC PW values (Figure 5a).

3.3. The 2009/2010 El Niño (Warm Event)

[20] When El Niño occurs, the equatorial Walker circulation will be reduced in response to weakening of northeasterly trade wind and causes the warm sea surface water east of Indonesia to move eastward. The equatorial central Pacific becomes warmer with more convective clouds triggered by upward motions. Over the equatorial western Pacific, the SST becomes relatively colder with sinking motions aloft and hence reduced precipitation. The warm event normally is strongest during the winter time [*Rasmusson and Carpenter*, 1982].

[21] Figure 3 shows the seasonal average of the winter months from December 2009 to February 2010 (the most intense phase of the warm event) for SST, precipitation rate, NCEP reanalysis PW, and the horizontal divergence of water vapor flux and horizontal wind at 850 hPa. Over the equatorial central Pacific, warmer SST coincides with higher precipitation rate, higher NCEP reanalysis PW, and convergence of horizontal water vapor flux. The PW computed from COSMIC RO data also exhibits larger amounts in the tropics (Figure 5d), while further concentrated near the equatorial central Pacific with a maximum of about 60 mm. In the warm event, larger PW zone is also extended to Amazon

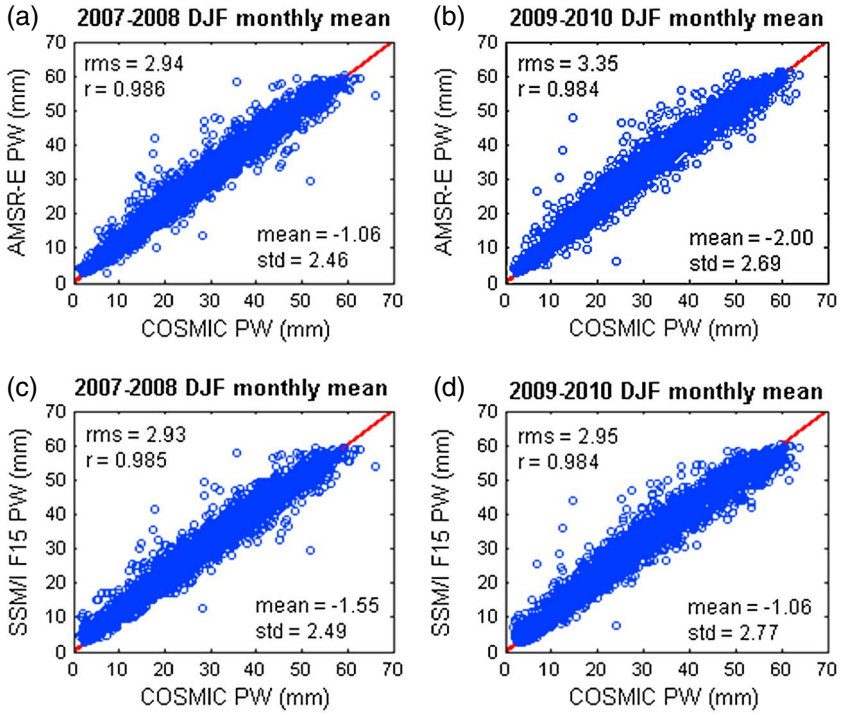

Figure 6. (a) Scatter plot of COSMIC PW and AMSR-E PW at collocated bins in 2007–2008 December–February (DJF) monthly mean, (b) same as Figure 6a but for 2009–2010 DJF monthly mean, (c) same as Figure 6a but for COSMIC and SSM/I F15, and (d) same as Figure 6c but for 2009–2010 DJF monthly mean. The root-mean-square differences, correlations, mean differences, and their standard deviations are given.

Basin (Figure 5d). The convergence zone of horizontal water vapor flux, as seen in Figure 3d, is also consistent with the region of larger PW where the equatorial easterly wind is reduced east of the date line during the winter months of the warm event. In general, these features are the characteristics of cloud convection associated with ITCZ. These results are consistent with previous investigations of the connection of sea surface temperature, atmospheric convection, and

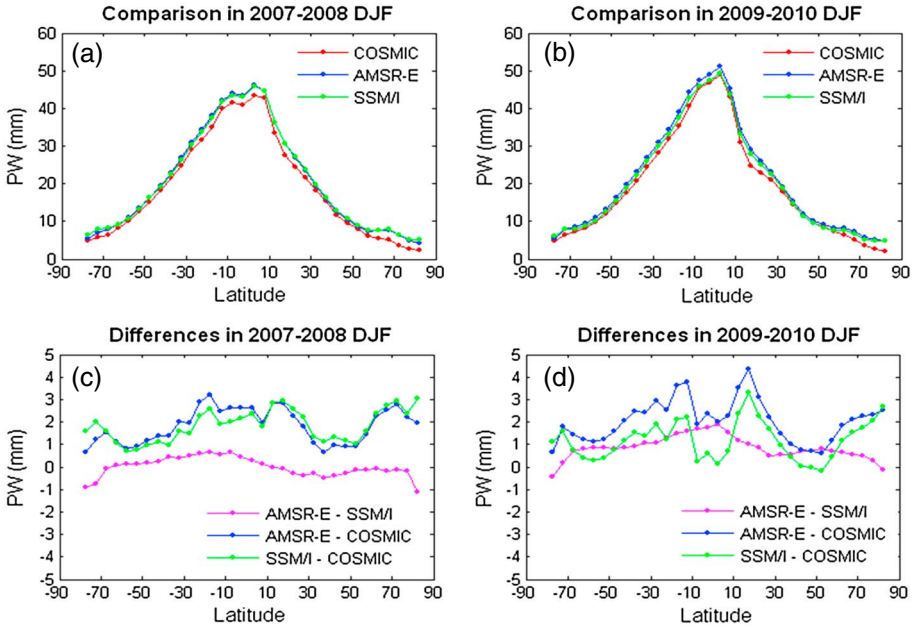

Figure 7. Zonal seasonal mean PW of COSMIC, AMSR-E, and SSM/I in the two periods (a) December 2007 to February 2008 (the cold ENSO event) and (b) December 2009 to February 2010 (the warm ENSO event). (c and d) as in Figures 7a and 7b, respectively, but for their differences.

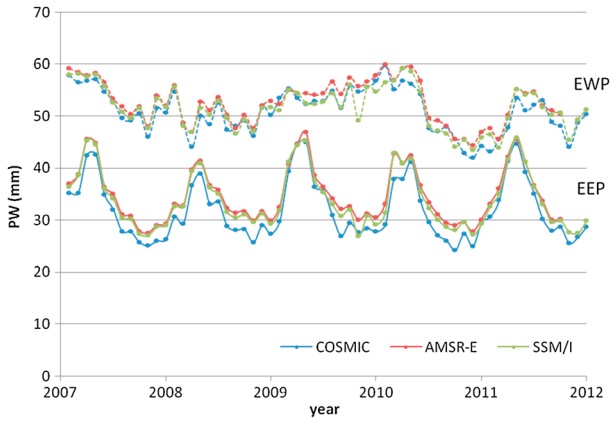

Figure 8. Time variations of monthly mean PW (mm) in 2007–2011 for COSMIC (blue), SSM/I (green), and AMSR-E (red). The upper and lower three curves are the PW averages in the equatorial western Pacific (EWP) (0°S–10°S, 150°E–170°E) and the equatorial eastern Pacific (EEP) (0°S–10°S, 120°W–140°W), respectively.

atmospheric humidity in regard to ENSO events (e.g., *Deser and Wallace*, 1990; *Lau et al*., 1998; *Trenberth et al*., 2002).

4. Global Inter-Satellite PW Comparisons for the ENSO Events

[22] Mean COSMIC PWs for ENSO cold and warm events during winter months (December, January, and February) are compared with those from AMSR-E and SSM/I. Comparison results are summarized in this section.

4.1. Inter-Satellite PW Comparisons

[23] Figure 4 depicts the latitudinal variations of the monthly mean PW for COSMIC, SSM/I, and AMSR-E from 2007 to 2011. The PW over oceans from NCEP global reanalysis is also provided for reference. All PWs show similar variations with time, normally with larger magnitude during the summer months and smaller magnitude in the winter time. The PW in the 2007–2008 winter months during the cold ENSO event exhibits a salient drop, while PW becomes larger in the 2009–2010 winter months during the warm phase of ENSO. These patterns are well captured by all the three satellite PW data sets and the NCEP global reanalysis. In general, the NCEP PW is in a good agreement with the satellite PWs except for smaller magnitudes over the tropical region and weaker latitudinal gradients in about 25°N–40°N. We should be aware of such underestimate by tropical NCEP PW since the other three satellite PWs are in good consistency. Besides, we note that the PW slopes are much steeper in the fall of 2009 for SSM/I, which are not seen by COSMIC and AMSR-E, and in the fall of 2010 for AMSR-E but not displayed by COSMIC and SSM/I. Therefore, we are skeptical about such steeper PW slopes during ending ENSO. Nevertheless, the consistent PW time series among the three satellite data sets clearly demonstrate the signals of convection activity associated with the cold and warm ENSO events.

[24] Figure 5 shows the global distribution of mean PW (mm) for each 5° × 5° grid point during the winter months for COSMIC, AMSR-E, and the PW differences between COSMIC and AMSR-E for the 2007/2008 cold event and 2009/2010 warm event. Since SSM/I PW is close to AMSR-E PW in magnitude and distribution, we only show the AMSR-E results here. For the cold event, both higher COSMIC and AMSR-E PWs are located in the vicinity of Indonesia and off eastern Australia (Figures 5a and 5b). The COSMIC PW shows a difference less than 5 mm, compared to AMSR-E PW over the entire oceans (Figure 5c). Slight positive differences between AMSR-E and COSMIC PWs occur over south Pacific (east of Australia) and the Indian Ocean. For the warm event, the COSMIC PW distributions are also similar to those of AMSR-E (Figures 5d and 5e), while the differences between AMSR-E and COSMIC PWs are generally within 5 mm and are small west of the equatorial central Pacific (Figure 5f). Larger differences in PW (darker colors) are over the tropical region where the maximum AMSR-E PW is about 55 mm.

[25] The scatter plots of monthly mean PW for COSMIC, SSM/I, and AMSR-E in 5° × 5° grids for three winter months are shown in Figure 6. The mean PW difference, root-mean-square (RMS) difference, correlation coefficient, and the standard deviation relative to the mean difference are also indicated. For the 2007/2008 cold event, the COSMIC PWs are highly correlated with those from SSM/I and AMSR-E with the correlation coefficients equal to 0.985 and 0.986, respectively. The RMS differences are less than 3 mm for both COSMIC-SSM/I pairs and COSMIC-AMSR-E pairs. The correlation coefficients computed here are close to those computed by *Wick et al*. [2008] (Figure 2) for the atmospheric river study. The standard deviations for the COSMIC-SSM/I pairs and COSMIC-AMSR-E pairs are equal to 2.49 mm and 2.46 mm, respectively. For the 2009/2010 warm event, the correlation coefficients for both COSMIC-SSM/I pairs and COSMIC-AMSR-E pairs are equal to 0.984 (see Figures 6b and 6d). Note that the above inter-satellite PW correlations are not for the coincident retrievals but for the monthly mean PW from COSMIC, SSM/I, and AMSR-E in the same 5° × 5° grid point.

[26] Figure 7 shows zonal seasonal mean PW and the differences among COSMIC, AMSR-E, and SSM/I in the two periods, December 2007 to February 2008 (the cold event) and December 2009 to February 2010 (the warm event). In general, PWs from these three satellites show very similar latitudinal variations. The PW differences between AMSR-E and SSM/I in general are much smaller than the differences between COSMIC and AMSR-E and between COSMIC and SSM/I. All the differences among COSMIC, AMSR-E, and SSM/I are within 3 mm outside the tropics and 5 mm inside the tropics. It is interesting to see very small differences between COSMIC and SSM/I within about 10° of the equator in the 2009/2010 warm event. Most of the COSMIC PW over oceans is lower than AMSR-E PW, but positive or smaller differences appear near the equator for the warm event. The characteristic result is also similar for COSMIC PW and SSM/I PW (not shown), probably leading to the smaller differences within 10° of the equator than outside. The fractional differences between COSMIC and the other satellites are below 20% in midlatitude and tropics (not shown). Largest differences between COSMIC and the other two satellites appear near 15°N in the 2009/2010 warm event. Such largest difference moves poleward to 20°N for the 2010–2011 winter months (2010/2011 cold event), but

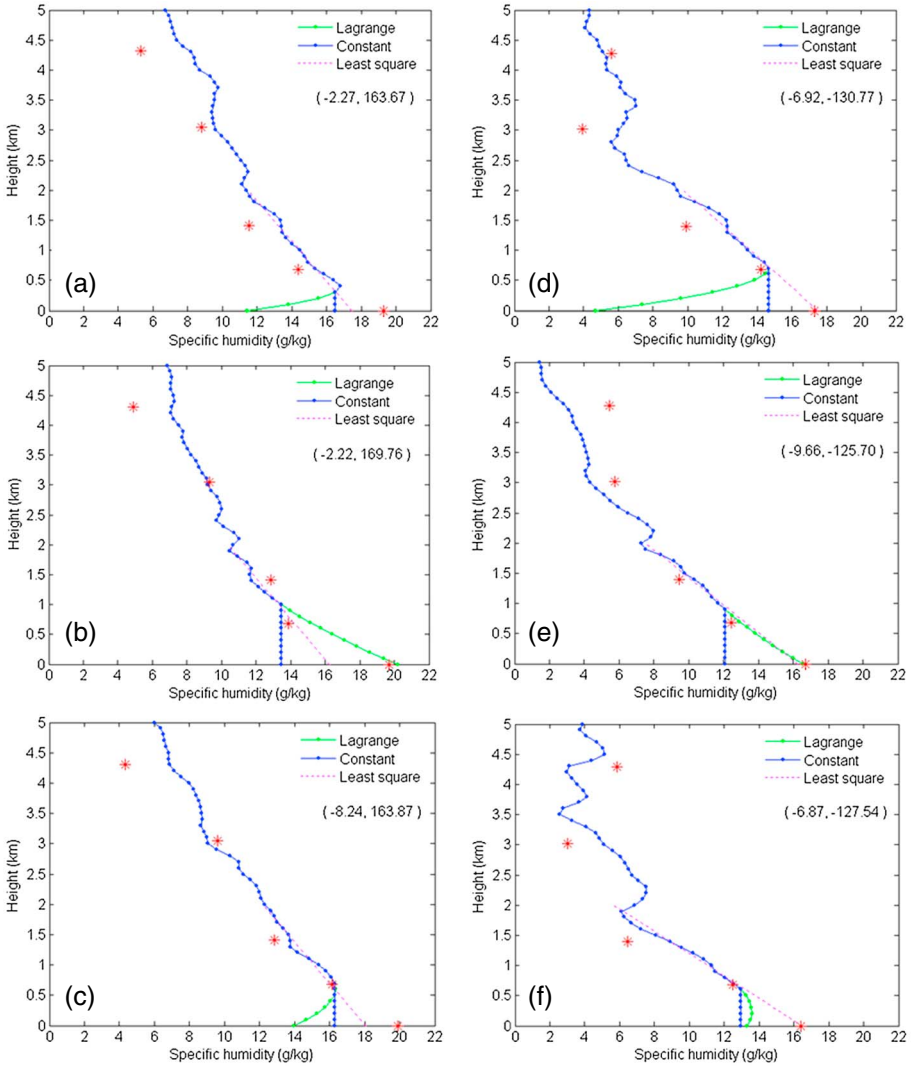

Figure 9. Vertical profiles of specific humidity from COSMIC in the equatorial western Pacific (0°S–10°S, 150°E–170°E) at (a) (2.27°S , 163.67°E), (b) (2.22°S , 169.76°E), and (c) (8.24°S , 163.87°E), and in the equatorial eastern Pacific (0°S–10°S, 120°W–140°W) at (d) (6.92°S, 130.77°W), (e) (9.66°S , 125.70°W), and (f) (6.87°S, 127.54°W) in February 2010. The green (pink) line indicates the extrapolated profile from the perigee height of the RO by a quadratic fit (a least-square fit). The red asterisks represent the coincident specific humidity from NCEP global reanalysis at the RO point.

with the maximum magnitude lowered to 3 mm (figures not shown).

[27] We further quantify the time series differences among COSMIC, SSM/I, and AMSR-E in the period of 2007–2011 for smaller local regions. We used the two selected regions in *Chou et al*. [2009], equatorial western Pacific region (EWP) (0°S–10°S, 150°E–170°E) and equatorial eastern Pacific region (EEP) (0°S–10°S, 120°W–140°W), which are approximate warm and cold pools, respectively. Note that the EEP partially overlaps with Niño 3.4 region (5°N–5°S, 120°–170°W). Figure 8 depicts the time series of the monthly mean PW for COSMIC, SSM/I, and AMSR-E. The three inter-satellite PW data sets exhibit similar interseasonal variation in both EWP and EEP, despite that COSMIC PW in EEP is somewhat lower than those from AMSR-E and SSM/I. The significant PW variations in EEP are associated with annual cycles. In EWP, the lower PW amounts in 2007–2008 and 2010–2011 winter months well correspond to the two cold ENSO events. The 2009/2010 warm event is demonstrated by prolonged high PW values from 2009 winter to 2010 spring. The annual cycle appears to be suppressed to a great extent in EWP. The detailed mechanism for such annual variations remains to be explored.

4.2. Sensitivity of the Compensation Below the Lowest Ray Perigee Height

[28] Although using COSMIC profiles with ray perigee height below 1 km in this study, the COSMIC PW dry biases relative to those from AMSR-E and SSM/I may result partially from specific methods to fill in water vapor values

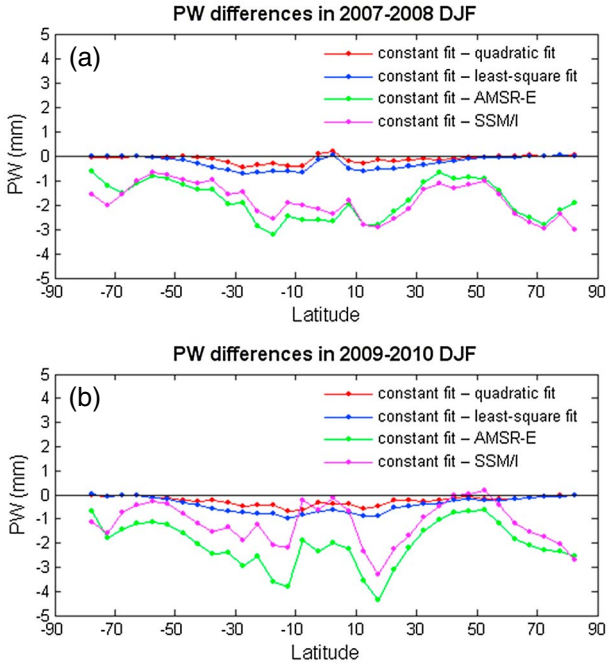

Figure 10. Zonal seasonal mean differences of PW between constant fit of COSMIC and AMSR-E, SSM/I, quadratic fit and least-square fit of COSMIC, respectively, in the two periods of (a) December 2007 to February 2008 (the cold ENSO event) and (b) December 2009 to February 2010 (the warm ENSO event).

below the lowest ray perigee point. Although the retrieved COSMIC water vapor above the lowest perigee point may be reasonably accurate, the COSMIC water vapor used below the lowest perigee point may introduce extra uncertainty for the computed COSMIC PW.

[29] From climatological comparisons, *Chou et al*. [2009] found that the COSMIC humidity is systematically smaller (larger) than AIRS humidity in the lower (upper) troposphere in three Pacific regions. In this study, we applied a simple compensation method for the layer of void RO data below which a constant profile is assumed for water vapor. This assumption may underestimate the PW, especially over the warm sea surface with higher saturated water vapor pressure. Thus, we conducted sensitivity experiments with other alternatives to fit the water vapor in the lowest layer with no RO measurement. For comparisons, we select a quadratic fit formulated by the lowest three RO points and a least-square fit determined by a linear regression of all the data points below 2 km height.

[30] We then examine the fitted vertical profiles of specific humidity from COSMIC in two chosen regions, EWP and EEP. Figure 9 shows six vertical profiles of specific humidity in EWP and EEP in February 2010. Note that these selected profiles are only a few representatives of the RO events associated with broad variabilities in the two regions. For reference, the coincident specific humidity from NCEP global reanalysis is also given at the RO location. The specific humidity profiles of NCEP and RO are in good agreement. It appears that the quadratic fit may work better than the constant fit to approach the surface reference value. However, the selected examples in EWP and EEP also indicate that a quadratic fit may result in a significant underestimate when there exists a large concave curvature (e.g., Figures 9a and 9d); in such a circumstance, a constant profile will reduce the deviation. As can be seen, the least-square fit works well among most of the cases, but sometimes it is inferior to the quadratic fit as seen in Figure 9b. The least-square fit will also suffer from a dramatic change above the boundary layer as shown in Figure 9f. We found that all the extrapolated fits become more problematic as the lowest ray perigee height is higher. This situation makes sampling of the RO profiles with the lowest perigee height below 1 km a reasonable choice.

[31] We examined the overall differences in PW using the three different fits for the 2007/2008 cold event and 2009/2010 warm event in Figure 10. In general, the differences of latitudinal monthly mean using different fits are only within 1 mm for the 2007/2008 cold event and slightly increase but still within 1 mm for the 2009/2010 warm event. The quadratic fit remedies some insufficiency of the constant fit for the two events, especially at lower latitudes. Except near the equator in the 2007/2008 cold event, the least-square fit tends to give more compensation as has been explained by some examples in Figure 9. However, the degree of such compensation with different fits is not appreciable so that sizable departures from AMSR-E and SSM/I PWs remain evident. The constant fit used in this study seems to be a reasonable approach as demonstrated in the inter-satellite PW comparisons.

5. PW Anomaly During the ENSO Events

[32] The above inter-satellite PW comparisons demonstrate the consistency among COSMIC, SSM/I, and AMSR-E PWs during the ENSO warm and cold events. As demonstrated in Figure 7, the seasonally averaged AMSR-E and SSM/I PWs in different latitudes are higher than COSMIC PW, regardless of the cold or warm event. This may indicate that PW could be systematically underestimated by COSMIC in a sense discussed earlier. However, such PW differences are small and do not render their PW distributions in the region of strong ENSO signals inconsistent. Hence, it is worth taking a look at their anomalies for schematics of global climate variability.

[33] Figure 11 shows seasonally averaged anomaly of PW during the three ENSO events for COSMIC and AMSR-E; the anomaly is defined by the PW departure in an ENSO event from the winter months (December 2008 to February 2009) in the neutral ENSO condition. Again, we herein omit the plots of SSM/I PW anomaly which are similar to those of AMSR-E. For both AMSR-E and SSM/I data, the same period is adopted here for a homogeneous comparison with COSMIC data. The COSMIC PW anomaly for the warm event exhibits a significant increase in the central Pacific, which is in good agreement with those from AMSR-E and SSM/I. Again, some noticeable COSMIC PW variations over lands, extended from the ocean part, present consistent ENSO signals for both oceans and lands which are not available from AMSR-E and SSM/I data. It appears that both COSMIC and AMSR-E show positive PW anomaly on South America and East Africa. On the other hand, for the 2007/2008 cold event, the COSMIC PW exhibits negative anomaly over the central Pacific, which is not as pronounced as for the other satellites. The signals of negative and positive PW anomalies in the Pacific for the three satellites are

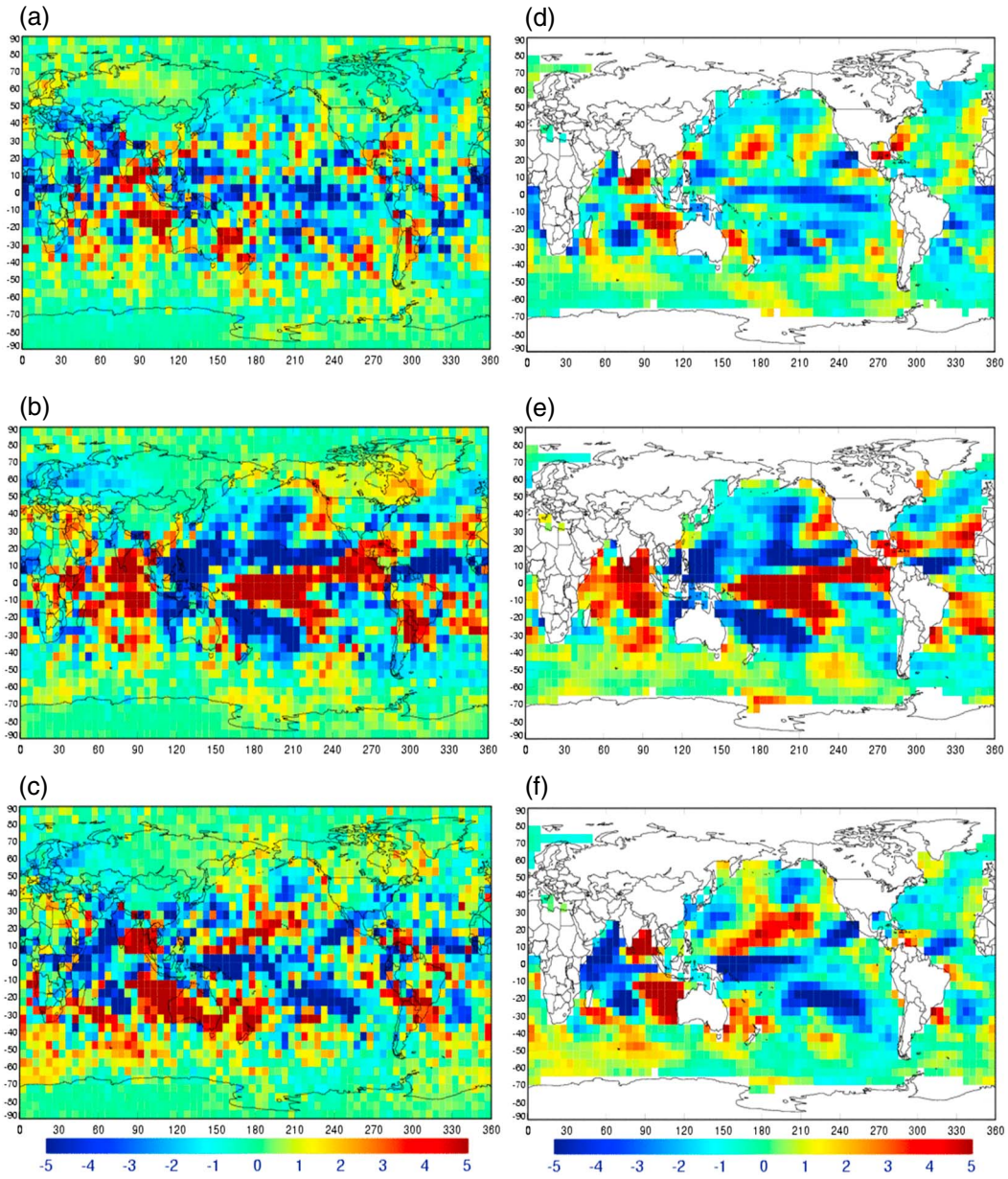

Figure 11. Anomaly of seasonal average PW (mm) in the winter months from COSMIC for (a) 2007 cold event, (b) 2009 warm event, (c) 2010 cold event; (d, e, and f) as in Figures 11a, 11b, and 11c, respectively, but from AMSR-E.

stronger in the 2010/2011 cold event, with appreciable enhancement east of Indonesia. As revealed by COSMIC, the large positive PW anomalies in fact occur in eastern Australia, where a historically torrential flood was reported by news.

[34] Figure 12 depicts scatter plots of PW anomaly for COSMIC, AMSR-E, and SSM/I during the three ENSO events. Despite that the inter-satellite monthly mean PW patterns are quite similar, their anomalies exhibit noticeable differences. The inter-satellite correlation coefficients for the PW anomaly for the 2007/2008 cold event are smaller than those for the 2009/2010 warm event, and the latter for COSMIC reaches about 0.9 in better correlations with AMSR-E and SSM/I than the former. The correlations were 0.7 for the 2007/2008 cold event and 0.8 for the stronger 2010/2011 event. Both AMSR-E and SSM/I PWs are in good agreement for all the three events, with correlation coefficients higher than 0.93. Using these two data sets as reference, the COSMIC PW anomaly appears to be higher and is considered to be "skewed." The skewness is reduced in the 2009/2010 warm event, as the regression slope is raised up closer to 1 in the scatter plots. These consistent inter-satellite correlations in ENSO signals, with respect to the winter months during neutral ENSO conditions, are encouraging since for such comparison with SSM/I and AMSR-E, COSMIC has only about 1150 RO profiles per day that reach lower than 1 km during 2007–2011.

6. Concluding Remarks

[35] With RO receivers on board six LEO satellites, COSMIC measurements provide rather uniform spatial and

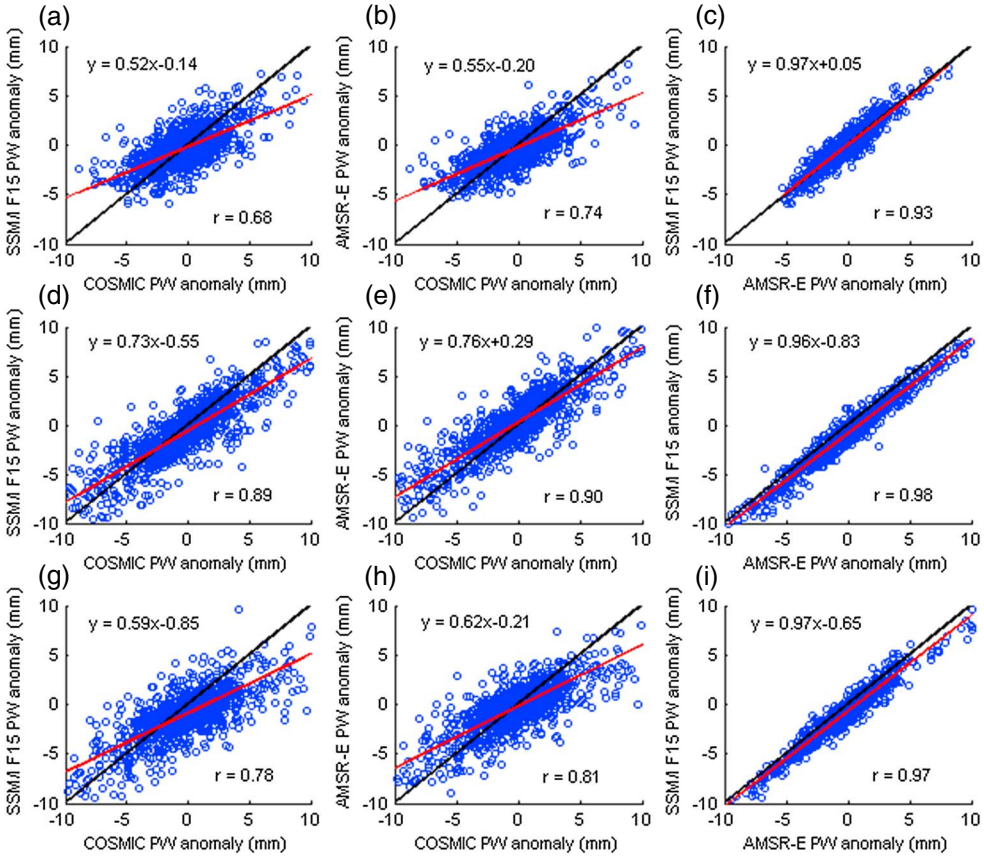

Figure 12. Scatter plots of anomaly of seasonal average PW (mm) at collocated bins in the winter months in the 2007 cold event for (a) COSMIC and SSM/I F15, (b) COSMIC and AMSR-E, and (c) SSM/I F15 and AMSR-E. (d, e, and f) As in Figures 12a, 12b, and 12c, respectively, but for the 2009 warm event. (g, h, and i) As in Figures 12a, 12b, and 12c, respectively, but for the 2010 cold event. Red line in each panel indicates the linear regression.

temporal distribution of profiles with a high vertical resolution of about a few hundred meters in the lower troposphere [*Anthes et al.*, 2008]. While the precision of COSMIC-derived temperature profiles is estimated to be better than 0.05 K from 8 km to 30 km [*Ho et al.*, 2009a], the COSMIC-retrieved moisture profiles are associated with observational errors within 0.2 g kg^{-1} in the lowest 2 km of the atmosphere when compared with ECMWF global analyses [*Ho et al.*, 2010a]. In this study, the characteristics of PW derived from COSMIC RO measurements are analyzed for different ENSO events. We focus on global PW variations associated with the ENSO warm (El Niño) and cold (La Niña) events from 2007 to 2011. The 5°×5° binned PW from COSMIC, AMSR-E, and SSM/I are compared. To compensate the missing part of PW below the lowest ray perigee height of COSMIC measurements, we simply assume a constant moisture profile below the lowest ray perigee height in this study.

[36] Information of samples collected in different ways may contain sampling errors as discussed in *Foelsche et al.* [2008]. Note that spatial and temporal sampling of COSMIC (with a uniform spatial and temporal coverage) and those of SSM/I and AMSR-E (with clustered measurement at fixed local times) are very different. In this study, we assume the (regional) diurnal variation of PW over oceans is reasonably small. Comparing to SSM/I and AMER-E PWs, the combined sampling error uncertainty and effect of extrapolating the water vapor values below the lowest penetration heights may introduce less than on average about 2 mm COSMIC PW biases (Figure 10). The mean COMIC PW biases, relative to those from AMSR-E and SSM/I, are obvious and are generally constant with latitudes (i.e., Figure 7) and are not dependent on the RO samples used in the same latitudinal zones. Although the COSMIC PW retrievals have dry biases (due to nature of retrieval and possible sampling error uncertainty compared to those from SSM/I and AMSR-E), after removing the systematic mean COSMIC PW, the PW anomalies from COSMIC are very consistent with those from AMSR-E and SSM/I (in Figures 11 and 12).

[37] Monthly zonal averaged COSMIC PW shows latitudinal variations with a small annual shift in the latitude of maximum intensity except for 2010 (the later phase of the warm event) in which peak PW of about 50 mm is closer to the equator. For the three ENSO events, we found that the COSMIC monthly mean PW is in a very high correlation (up to 0.98) with those from SSM/I and AMSR-E over the ocean, with RMS differences less than 4 mm. The PWs from the three different satellites also have similar latitudinal variations. However, the PW is somewhat underestimated by GPS RO, in particular, in the tropical regions where ITCZ is active. This underestimate is caused by the fact that not all RO measurements can reach the surface, which cannot be fully complemented for PW by assuming an extrapolated

moisture profile below the RO perigee height. Nevertheless, the inter-satellite PW comparisons are reasonably good, providing useful verification of the accuracy of COSMIC PW. The global seasonal distributions of COSMIC PW associated with the ENSO events exhibit high correlation with observed precipitation rate over the ocean. Cloud convection with maximum PW moved to the equatorial central Pacific in the winter months of the warm event, while it shifted to the Indonesian region of the western Pacific in the cold event. The results are consistent with previous investigations of the connection of sea surface temperature, atmospheric convection, and atmospheric humidity in regard to ENSO events [*Rasmusson and Carpenter*, 1982; *Deser and Wallace*, 1990; *Wang et al*., 2000].

[38] Based on ONI, the year of July 2008 to June 2009 is defined as a neutral ENSO condition in this study. The reverse phases in the Walker circulation are prominent for the warm and cold events, and the chosen neutral ENSO condition should be a justified period deliverable to extract the PW anomaly information to a first approximation. The COSMIC PW is thus applied to detect the global variability associated with the ENSO events. In comparisons with PW of the other two satellites, COSMIC PW is capable of displaying the ENSO signals with major PW anomaly near the central Pacific in the 2009/2010 warm event and near the Indonesian region and east of Australia in the 2007/2008 and 2010/2011 cold events. However, the 2007/2008 La Niña signals are somewhat less pronounced for COSMIC as compared to AMSR-E and SSM/I. For the 2010/2011 La Niña, their signals are in better agreement. In general, the inter-satellite PW anomaly patterns nicely concur on major ENSO signals. The correlations of PW anomaly for all global bins between COSMIC and AMSR-E as well as COSMIC and SSM/I can reach about 0.9 for the 2009/2010 warm event.

[39] We have looked into a 5 year trend of inter-satellite PW from 2007 to 2011. In the selected approximate cold pool and warm pool regions defined in this study over the equatorial Pacific, PW retrievals from COSMIC, SSM/I, and AMSR-E show very similar trends in their monthly mean. Again, COSMIC PW is slightly less in the cold pool as compared to SSM/I and AMSR-E. A strong annual cycle is evident in the cold pool while diminishing in the warm pool, although not completely. This weakened annual cycle in the warm pool might be related to continental weather activities nearby. All the three inter-satellite PWs indicate a reduced peak in the cold pool and a raised peak in the warm pool during the 2009/2010 warm event. In summary, these inter-satellite comparisons show a consistent trend of latitudinal variations in monthly mean PW from 2007 to 2011 that displays similar ENSO signals in the cold and warm events.

[40] In a sensitivity study, the presumed constant moisture profile below the lowest RO perigee height has been remedied by a quadratic profile or a least-square fit. However, we found that the underestimate on PW by COSMIC was not significantly improved over most of the oceanic regions due to that the mathematical extrapolation might not have intimately reflected the physical variations in the boundary layer. A robust method should be developed to capture natural moisture variation in the boundary layer in order to facilitate use of RO data. Increased profiles further down to near the surface and more RO observations in low latitudes are also helpful for studying global climate variability. A COSMIC follow-on mission (i.e., COSMIC-II, a collaboration between US and Taiwan) has commenced to prepare a first launch in 2016 with six LEOs at a declination angle of 24° and should provide many more RO observations in the tropical regions.

[41] **Acknowledgments.** This study was supported by National Space Program Organization (NSPO) in Taiwan. The leading author is grateful for the support of NSPO for a visit to UCAR/COSMIC. Valuable comments on this study by Prof. M.-D. Chou are appreciated.

References

Anthes, R. A., et al. (2008), The COSMIC/FORMOSAT-3 Mission: Early results, *Bull. Amer. Meteor. Soc.*, *89*, 313–333.

Anthes, R. A. (2011), Exploring Earth's atmosphere with radio occultation: Contributions to weather, climate and space weather, *Atmos. Meas. Tech.*, *4*, 1077–1103, doi:10.5194/amt-4-1077-2011.

Arndt, D. S., M. O. Baringer, and M. R. Johnson, Eds. (2010), State of the Climate in 2009, *Bull. Amer. Meteor. Soc.*, *91*(7), S1–S224.

Bean, B. R., and E. J. Dutton (1966), Radio Meteorology, National Bureau of Standards, *Monogr*., No. 92, U.S. Government Printing Office, 435 pp.

Chou, M.-D., C.-H. Weng, and P.-H. Lin (2009), Analysis of FORMOSAT-3/COSMIC humidity retrievals and comparisons with AIRS retrievals and NCEP/NCAR reanalysis, *J. Geophys. Res.*, *114*, D00G03, doi:10.1029/2008JD010227.

Deser, C., and J. M. Wallace (1990), Large-scale atmospheric circulation features of warm and cold episodes in the tropical Pacific, *J. Climate*, *3*, 1254–1281.

Foelsche, U., M. Borsche, A. K. Steiner, A. Gobiet, B. Pirscher, G. Kirchengast, J. Wickert, and T. Schmidt (2008), Observing upper troposphere-lower stratosphere climate with radio occultation data from the CHAMP satellite, *Clim. Dyn.*, *31*, 49–65, doi:10.1007/s00382-007-0337-7.

Hajj, G., C. O. Ao, B. A. Iijima, D. Kuang, E. R. Kursinski, A. J. Mannucci, T. K. Meehan, L. J. Romams, M. de la Torre Juarez, and T. P. Yunck (2004), CHAMP and SAC-C atmospheric occultation results and inter-comparisons, *J. Geophys. Res.*, *109*, D06109, doi:10.1029/2003JD003909.

Healy, S. B., and J. R. Eyre (2000), Retrieving temperature, water vapour and surface pressure information from refractive-index profiles derived by radio occultation: A simulation study, *Q. J. R. Meteorol. Soc.*, *126*, 1661–1683.

Healy, S. B., J. R. Eyre, M. Hamrud, and J.-N. Th´epaut (2007), Assimilating GPS radio occultation measurements with two-dimensional bending angle observation operators, *Q. J. R. Meteor. Soc.*, *133*, 1213–1227, doi:10.1002/qj.63.

Ho, S.-P., Y.-H. Kuo, Z. Zeng, and T. C. Peterson (2007a), A comparison of lower stratosphere temperature from microwave measurements with CHAMP GPS RO data, *Geophys. Res. Lett.*, *34*, L15701, doi:10.1029/2007GL030202.

Ho, S.-P., Y.-H. Kuo, and S. Sokolovskiy (2007b), Improvement of the temperature and moisture retrievals in the lower troposphere using AIRS and GPS radio occultation measurements, *J. Atmos. Oceanic Technol.*, *24*, 1726–1739, doi:10.1175/JTECH2071.1.

Ho, S.-P., M. Goldberg, Y.-H. Kuo, C.-Z. Zou, W. Schreiner (2009a), Calibration of temperature in the lower stratosphere from microwave measurements using COSMIC radio occultation data: Preliminary results, *Terr. Atmos. Oceanic Sci.*, *20*, doi:10.3319/TAO.2007.12.06.01(F3C).

Ho, S.-P., et al. (2009b), Estimating the uncertainty of using GPS radio occultation data for climate monitoring: Inter-comparison of CHAMP refractivity climate records 2002–2006 from different data centers, *J. Geophys. Res.*, D23107, doi:10.1029/2009JD011969.

Ho, S.-P., X. Zhou, Y.-H. Kuo, D. Hunt, and J.-H. Wang (2010a), Global evaluation of radiosonde water vapor systematic biases using GPS radio occultation from COSMIC and ECMWF analysis, *Remote Sens.*, *2*, 1320–1330, doi:10.3390/RS2051320.

Ho, S.-P., Y.-H. Kuo, W. Schreiner, and X. Zhou (2010b), Using SI-traceable global positioning system radio occultation measurements for climate monitoring [In "State of the Climate in 2009"], *Bull. Amer. Meteor. Soc.*, *91*(7), S36–S37.

Ho, S.-P., et al. (2012), Reproducibility of GPS radio occultation data for climate monitoring: Profile-to-profile inter-comparison of CHAMP climate records 2002 to 2008 from six data centers, *J. Geophys. Res.*, *117*, D18111, doi:10.1029/2012JD017665.

Kalnay, E., et al. (1996), The NCEP/NCAR 40-year reanalysis project, *Bull. Amer. Meteor. Soc.*, *77*, 437–471.

Kuo, Y.-H., T.-K. Wee, S. Sokolovskiy, C. Rocken, W. Schreiner, D. Hunt, and R. A. Anthes (2004), Inversion and error estimation of GPS radio occultation data, *J. Meteor. Soc. Japan*, *82*(1B), 507–531.

Kursinski E., G. A. Hajj, J. Schofield, R. Linfield, and K. Hardy (1997), Observing Earth's atmosphere with radio occultation measurements using the Global Positioning System, *J. Geophys. Res.*, *102*: 23,429–23,465.

Kursinski, E. R., G. A. Hajj, S. S. Leroy, and B. Herman (2000), The GPS radio occultation technique, *Terr. Atmos. Oceanic Sci.*, *11*, 53–114.

Lau, K. M., C. H. Ho, and I. S. Kang (1998), Anomalous atmospheric hydrologic processes associated with ENSO: Mechanisms of hydrologic cycle radiation interaction, *J. Climate*, *11*, 800–815.

Mears, C., J. Wang , S.-P. Ho, L. Zhang, and X. Zhou (2010), Total column water vapor [In "State of the Climate in 2009"], *Bull. Amer. Meteor. Soc.*, *91*(7), S29–S31.

Mears, C., J. Wang , S.-P. Ho, L. Zhang, and X. Zhou (2012), Total column water vapor [In "State of the Climate in 2011"], *Bull. Amer. Meteor. Soc.*, *93*(7), S44–S45.

Rasmusson, E. M., and T. H. Carpenter (1982), Variation in tropical sea surface temperature and surface wind fields associated with the southern oscillation/ El Niño, *Mon. Wea. Rev.*, *110*, 354–384.

Steiner, A. K., B. C. Lackner, F. Ladstädter, B. Scherllin-Pirscher, U. Foelsche, and G. Kirchengast (2011), GPS radio occultation for climate monitoring and change detection, *Radio Sci.*, *46*, RS0D24, doi:10.1029/2010RS004614.

Sohn, B.-J., and E. A. Smith (2003), Explaining sources of discrepancy in SSM/I water vapor algorithms, *J. Clim.*, *16*, 3229–3255.

Sokolovskiy, S., Y.-H. Kuo, C. Rocken, W. S. Schreiner, D. Hunt, and R. A. Anthes (2003), Effect of superrefraction on inversions of radio occultation signals in the lower troposphere, *Radio Sci.*, *38*(3), 1058, doi:10.1029/2002RS002728.

Sokolovskiy, S., Y.-H. Kuo, C. Rocken, W. S. Schreiner, D. Hunt, and R. A. Anthes (2006), Monitoring the atmospheric boundary layer by GPS radio occultation signals recorded in the open-loop mode, *Geophys. Res. Lett.*, *33*, L12813, doi:10.1029/2006GL025955.

Trenberth, K. E., J. M. Caron, D. P. Stepaniak, and S. Worley (2002), Evolution of El Niño–Southern Oscillation and global atmospheric surface temperatures, *J. Geophys. Res.*, *107*(D8), 4065, doi:10.1029/2000JD000298.

von Engeln, A., and G. Nedoluha (2005), Retrieval of temperature and water vapor profiles from radio occultation refractivity and bending angle measurements using an optimal estimation approach: A simulation study, *Atmos. Chem. Phys.*, *5*, 1665–1677.

Wang, B., R.-G. Wu, and X.-F. Fu (2000), Pacific-East Asia teleconnection: How does ENSO affect East Asia climate? *J. Climate*, *13*, 1517–1536.

Wang, J., L. Zhang, A. Dai, T. Van Hove, and J. Van Baelen (2007), A near-global, 8-year, 2-hourly data set of atmospheric precipitable water from ground-based GPS measurements, *J. Geophys. Res.*, *112*, D11107, doi:10.1029/2006JD007529.

Ware, R., et al. (1996), GPS sounding of the atmosphere from low earth orbit: Preliminary results, *Bull. Amer. Meteor. Soc.*, *77*, 19–40.

Wentz, F. J. (1993), Revision 2 user's manual SSM/I antenna temperature tapes, *RSS Technical Report 120193*.

Wentz, F. J. (1997), A well calibrated ocean algorithm for Special Sensor Microwave/Imager, *J. Geophys. Res.*, *102*, 8703–8718.

Wick, G. A., Y.-H. Kuo, F. M. Ralph, T.-K. Wee, and P. J. Neiman (2008), Intercomparison of integrated water vapor retrievals from SSM/I and COSMIC, *Geophys. Res. Lett.*, *35*, L21805, doi:10.1029/2008GL035126.